CHIN. PHYS. LETT. Vol. 38, No. 9 (2021) 097201

Simultaneous Optimization of Power Factor and Thermal Conductivity towards High-Performance InSb-Based Thermoelectric Materials

Wang Li(李旺), Tian Xu(许天), Zheng Ma(马征), Abubakar-Yakubu Haruna, Qing-Hui Jiang(姜庆辉), Yu-Bo Luo(罗裕波)*, and Jun-You Yang(杨君友)*

State Key Laboratory of Materials Processing and Die & Mould Technology, Huazhong University of Science and Technology, Wuhan 430074, China

(Received 1 August 2021; accepted 13 August 2021; published online 2 September 2021)

Thermoelectric performance of InSb is restricted by its low Seebeck coefficient and high thermal conductivity. Here, CuCl is employed to optimize simultaneously the electrical and thermal transport properties of InSb. The substitution of Cl for Sb results in enhanced electron effective mass, leading to high Seebeck coefficient of $-159.9\,\mu V/K$ and high power factor of $31.5\,\mu W\cdot cm^{-1}\cdot K^{-2}$ at 733 K for InSb + 5 wt% CuCl sample. In addition, CuCl doping creates hierarchical architectures composed of Cu_9In_4, Sb, Cu_2Sb in InSb, leading to a strengthened phonon scattering in a wide wavelength (i.e., nano to meso scale), thus a low lattice thermal conductivity of $2.97\,W\cdot m^{-1}\cdot K^{-1}$ at 733 K in InSb + 5 wt% CuCl. As a result, a maximum ZT of 0.77 at 733 K has been achieved for the InSb + 5 wt% CuCl sample, increasing by ∼250% compared to pristine InSb.

DOI: 10.1088/0256-307X/38/9/097201

Thermoelectric (TE) materials, which can convert heat to electricity or vice versa, become more and more important in energy conservation. The conversion efficiency of a TE device is determined by thermoelectric figure-of-merit $ZT = S^2T/\rho\kappa = S^2T/\rho(\kappa_L + \kappa_e)$, where S, ρ, κ_L, κ_e are the Seebeck coefficient, electrical resistivity, the lattice part and electronic part contributing to thermal conductivity, respectively.[1–3] Due to the close relation among S, ρ and κ_e via carrier concentration, it is of great challenge to obtain a significant ZT improvement through only one optimization of three parameters. Numerous efforts have been made to tackle this tough problem, such as first principle calculation,[4,5] low dimension strategies[6–8] and new materials synthesis methods.[9] Several classical high performance TE materials have been developed and many encouraging advances have been made in the past decades.[10] Unfortunately, materials used for thermoelectric generator at medium temperature are dominant by Pb based compounds, which are harmful to our environment and unsuitable for large scale applications. To date, many works have been focused on exploring candidates with environmental-friendly elements.[11–16]

InSb, a direct bandgap compound with the NiAs-type crystal structure (with a space group of $F\bar{4}3m$). It has been reported recently as a great potential in medium temperature thermoelectric application.[17] However, the InSb compound has a high thermal conductivity (∼17 $W\cdot m^{-1}\cdot K^{-1}$ at room temperature[18]), which largely limits its thermoelectric performance. To reduce the thermal conductivity, many works have been carried out. Su *et al.* reported a 16.6% decrease of κ_L by fabricating the InSb compound with the melt spinning method.[19] Moreover, Ga doping[20] and Te doping[21] in InSb have also been proved to be effective for reducing κ_L, which results in ∼63% and ∼74% reduction in κ_L due to the extra phonon scattering from Ga-poor nano-particles and In vacancies, respectively. Our previous works revealed a sharp decrease in κ_L stemmed from the eutectic remelting at 753–773 K.[22,23] Even so, the κ_L is still large ($>2\,W\cdot m^{-1}\cdot K^{-1}$) when $T < 723$ K. In addition, the Seebeck coefficient of InSb is lower ($|S| < 120\,\mu V/K$ at 303–723 K) compared with other classical high performance TE materials.[24–26] Therefore, reducing the thermal conductivity and enhancing the Seebeck coefficient of InSb are highly desirable to optimize its thermoelectric performance.

In this Letter, CuCl is used as an effective additive to improve the electrical and thermal transport properties of InSb. On the one hand, the substitution of Cl for Sb results in an increase in carrier concentration owing to the electron donor nature of Cl_{Sb}^{2+} point defects, and the substitution of Cl for Sb enhanced the Seebeck coefficient as a result of enhancement in electron effective mass induced by less dispersive electron band. On the other hand, hierarchical architectures composed of mesoscale Cu_2Sb, nanoscale Sb (∼50 nm) and Cu_9In_4 (10–20 nm) result in an obvious reduc-

Supported by the National Natural Science Foundation of China (Grant Nos. 52002137, 51772109, 51872102, and 51802070), the Fundamental Research Funds for the Central Universities (Grant Nos. 2021XXJS008 and 2018KFYXKJC002), and Graduates' Innovation Fund of Huazhong University of Science and Technology (Grant No. 2020yjsCXCY022).
*Corresponding authors. Email: luoyubo@hust.edu.cn; jyyang@mail.hust.edu.cn
© 2021 Chinese Physical Society and IOP Publishing Ltd

tion in lattice thermal conductivity of InSb due to the strengthened phonon scattering at 650–700 K. As a consequence, the InSb + 5 wt% CuCl sample achieves a maximum ZT of 0.77 at 723 K, which is about 250% higher than that of the pristine InSb.

InSb samples were prepared by high temperature (923 K) melting. The obtained ingots were crushed into fine powders and passed through 200-mesh sieve. Then, CuCl powders were added into InSb with different weight ratios x% (x = 0, 3, 5, 8). The powder mixtures were then subjected to spark plasma sintering (SPS) under a pressure of 60 MPa in vacuum atmosphere to get densified pellets. The characterization methods and specific equipment information are given in the Supplementary Material.

Figure 1 displays the powder x-ray diffraction (XRD) patterns of the InSb + x wt% CuCl (x = 0, 3, 5, 8) samples. The main Bragg diffraction peaks of all the samples match well with the NiAs-type InSb (PDF 06–0208). It is noted that no CuCl peak can be observed within the detection limit of the XRD measurements, but Bragg peaks of elemental Sb (PDF 35–0732) appear in the samples when the weight fraction of CuCl is more than 3%. The contents of Sb in the InSb + x wt% CuCl (x = 3, 5, 8) samples are estimated by Rietveld refinement (Fig. S1, Table S1), which increases with the increasing x, i.e., 0.3%, 3.1% and 6.0% for the x = 3, 5, 8 samples.

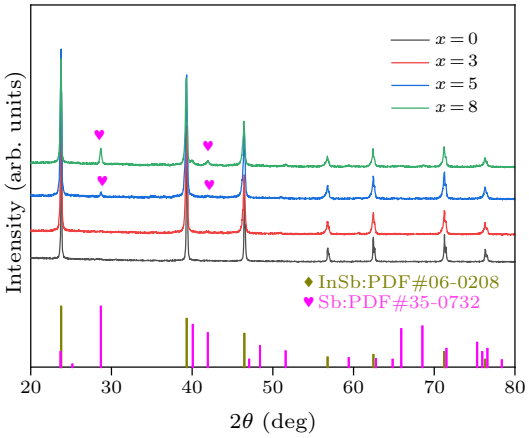

Fig. 1. Powder XRD patterns of the InSb + x wt% CuCl (x = 0, 3, 5, 8) samples.

Electron probe microanalysis (EPMA) was carried out to better understand the microstructure of the CuCl doped InSb, i.e., InSb + 8 wt%CuCl. Back-scattering electronic (BSE) image [Fig. 2(a)] shows some dark particles in the grey InSb matrix defined by energy dispersive x-ray spectroscopy (EDS) spot-1 results in Fig. 2(b). Wavelength dispersive spectrometer (WDS) mapping images of Cu and Sb in Figs. 2(c) and 2(d) further confirm that the grey particles mainly consist of Cu and Sb elements. EDS spot-2 results reveal that the composition of such grey particles is Sb : Cu = 31.61 : 67.76, closed to 1 : 2. Therefore, we speculate such grey particles to be Cu_2Sb. In addition, considerable Sb precipitates [marked in blue circles in Fig. 2(e)] sized in nanometers can be observed in the sample. It is worth noting that the Cl atoms distribute uniformly in the sample [Fig. 2(f)], indicating the successful substitution of Cl for Sb sites; while the Cu atoms cannot dissolve into InSb according to our WDS measurement, see Fig. 2(c).

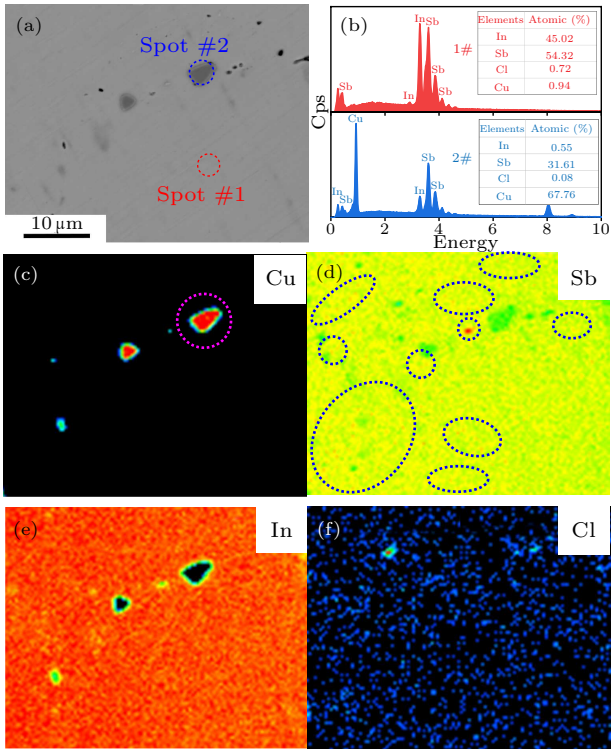

Fig. 2. (a) Back-scattering electronic (BSE) image of polished surface; (b) energy dispersive x-ray spectroscopy (EDS) analysis of spots in panel (a); (c)–(f) wavelength dispersive x-ray spectroscopy (WDS) mapping results of panel (a).

To further reveal the structure and composition of the InSb + 8 wt%CuCl sample, transmission electrical microscopy (TEM) characterization was carried out and the results are shown in Fig. 3. Dislocations and nanoscale Sb particles (∼50 nm) embedded in InSb matrix can be well observed [Fig. 3(a)], in line with our EPMA results. The corresponding selected area electron diffraction (SAED) pattern indicates that the precipitates are Sb secondary phase (red dots) taken along the [010] axis, as shown in Fig. 3(b). More importantly, large amounts of precipitates sized in several nanometers are observed in InSb matrix, as shown in Fig. 3(c). High-angle annular dark field (HAADF), Fig. 3(d), image and EDS mapping indicate that such nanoprecipitates are mainly composed of Cu and In elements. To further characterize its nature, fast Fourier transform (FFT) was carried out and the result reveals that such nanoprecipitates should be the Cu_9In_4 compound with a cubic structure, which is also consistent with the spot composition analysis

(Fig. S2).

According to the above XRD, EPMA and TEM results, one can see that CuCl doping results in the formation of mesoscale Cu_2Sb and nanoscale Sb (∼50 nm) and Cu_9In_4 (10–20 nm), namely hierarchical architectures. Therefore, we speculate the following reaction occurring during the SPS process of CuCl doped InSb:

$$15x\mathrm{CuCl} + (5+4x)\mathrm{InSb} = 5\mathrm{InSb}_{1-x}\mathrm{Cl}_{3x} + x\mathrm{Cu_9In_4} + 3x\mathrm{Cu_2Sb} + 6x\mathrm{Sb}. \quad (1)$$

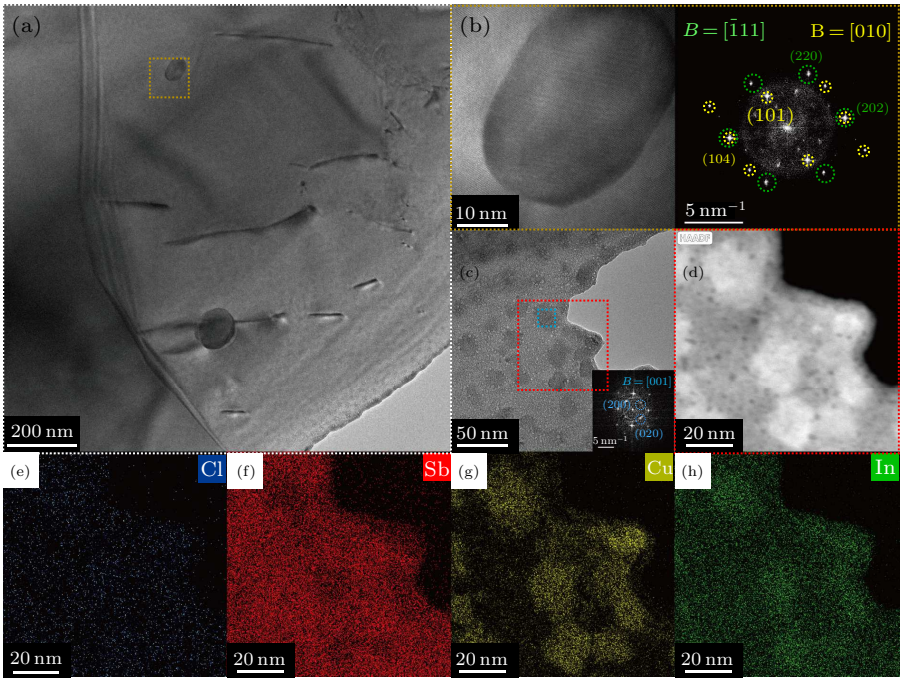

Fig. 3. Transmission electrical microscopy (TEM) observation of the dense bulk sample for $x = 8$. (a) Low-magnification TEM image of the sample; (b) HRTEM of enlarged image for the area highlighted by yellow dotted line and the corresponding SEAD pattern; (c) a representative area of the matrix, and the inset picture is FFT from the green dotted rectangle; (d) HAADF image of selected area highlighted by red dotted line in (c); (e)–(h) EDS mapping images of (d).

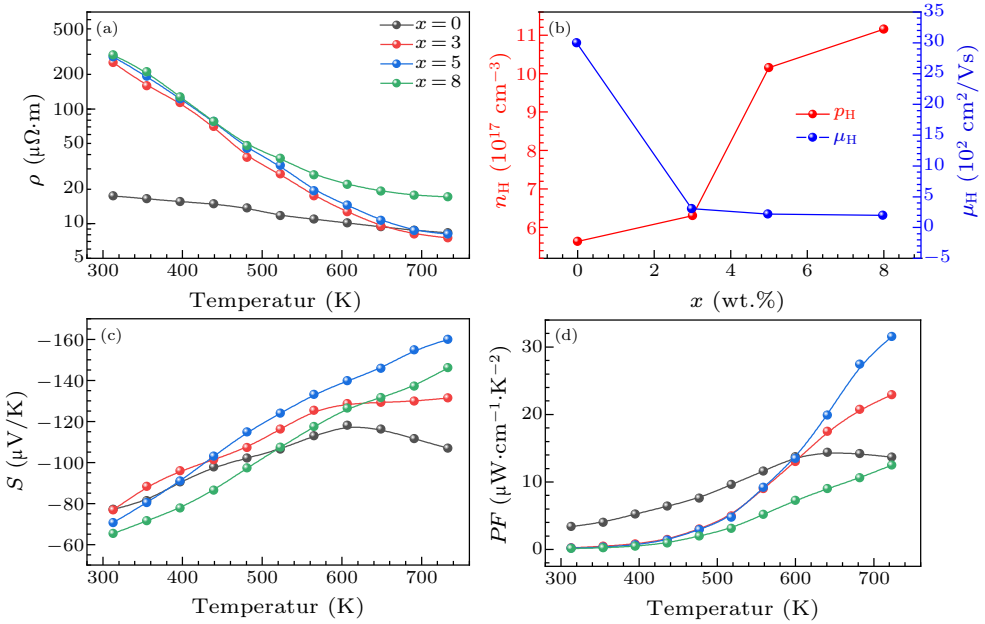

Fig. 4. (a) Temperature dependent ρ for InSb + x wt% CuCl ($x = 3, 5, 8$). (b) Hall carrier concentration (n_H) and mobility (μ_H) vs x. (c) Temperature dependent S for InSb + x wt% CuCl. (d) Temperature dependent power factor (PF) for InSb + x wt% CuCl ($x = 3, 5, 8$).

Figure 4 displays the ρ and S versus temperature for InSb + x wt% CuCl (x = 0 3, 5, 8). The ρ for all the samples decreases with the temperature increasing, indicating a semiconductor behavior. For instance, the ρ of InSb decreases from 17.5 μΩ·m at 313 K to 8.34 μΩ·m at 733 K. In addition, CuCl doping results in an increase in the electrical resistivity of InSb. For instance, the room-temperature ρ of InSb increases from 17.5 μΩ·m for the pristine sample to 306 μΩ·m for the $x = 8$ sample. Our Hall effect measurements show that the main reason for such an increase in ρ is the reduction in carrier mobility resulted from CuCl doping, as shown in Fig. 4(b). The Seebeck coefficients of InSb + x wt% CuCl (x = 0, 3, 5, 8) are negative, reflecting their n-type conduction nature. The absolute value S for pristine InSb increases from 76 μV/K at 313 K to 116 μV/K at 600 K and then decreases to the 107 μV/K at 733 K, which is due to the well-known bipolar diffusion, as shown in Fig. 4(c). After CuCl doping, the room temperature S of InSb deceases with the increasing CuCl content, which can be explained by the increase in carrier concentration owing to the substitution of Cl for Sb. In addition, the S of InSb + x wt% CuCl (x = 0, 3, 5, 8) is higher than the pristine InSb at 600–733 K. We ascribe this enhancement to the increased electron effective mass[27] which is estimated with the carrier concentration and S value at 313 K, according to the SPB model.[25] The calculation details are given in the Supplementary Material. The electron effective masses are 0.025 m_e, 0.026 m_e, 0.034 m_e, and 0.034 m_e for the x = 0, 3, 5, 8 samples, respectively, which are closed to that of previous research on InSb.[28] Such an increase in effective mass results from the less dispersive electron band due to Cl doping.[29] Figure 4(d) shows the power factor (PF) of the InSb + x wt% CuCl (x = 0, 3, 5, 8) samples. Specifically, for the $x = 5$ sample, the PF is lower than that of the pristine one at 313–600 K due to its higher ρ than InSb, but is higher than the pristine InSb at 600–733 K due to the increase in Seebeck coefficient. Finally, a high value of 31.5 μW·cm^{-1}·K^{-2} is reached at 733 K for the $x = 5$ sample, 123% higher than the pristine one (14.1 μW·cm^{-1}·K^{-2}).

Figure 5(a) shows the thermal conductivity κ for the InSb + x wt% CuCl (x = 0, 3, 5, 8) samples. The κ of InSb decreases from 10.3 W·m^{-1}·K^{-1} at 313 K to 4.6 W·m^{-1}·K^{-1} at 733 K. By CuCl doping, the κ of x = 3, 5, 8 samples are higher than that of the pristine InSb at 313–650 K, but is lower than the pristine InSb at 650–733 K. For example, the κ values are 11.64 W·m^{-1}·K^{-1}, 11.8 W·m^{-1}·K^{-1} and 10.6 W·m^{-1}·K^{-1} for the x = 3, 5, 8 samples at 313 K, and are 2.93 W·m^{-1}·K^{-1}, 2.99 W·m^{-1}·K^{-1} and 2.63 W·m^{-1}·K^{-1} for the x = 3, 5, 8 samples at 733 K, respectively. The electronic thermal conductivity values of all the samples were calculated by $\kappa_e = LT/\rho$, where L was estimated by experimental S data according to the single parabolic band (SPB) model,[25] as shown in Fig. S3(a). The κ_e increases with temperature for all the samples owing to the decrease in electrical resistivity with increasing temperature [Fig. S3(b)].

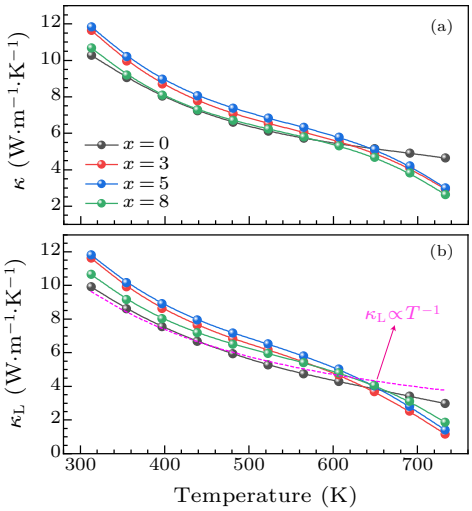

Fig. 5. (a) Temperature-dependent thermal conductivity κ and (b) lattice thermal conductivity κ_L of the InSb + x wt% CuCl samples (x = 0, 3, 5, 8).

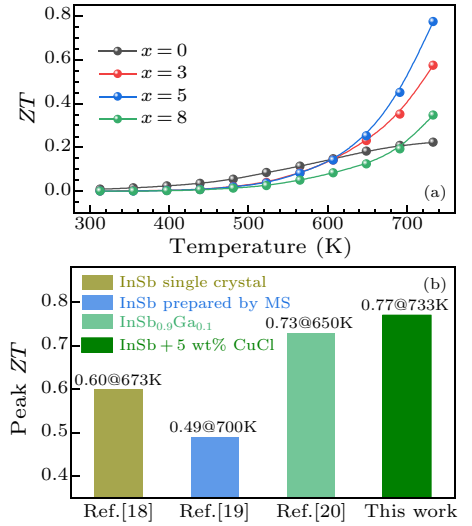

Fig. 6. (a) Temperature dependent ZT values for InSb + x wt% (x = 0, 3, 5, 8) CuCl; (b) peak ZT of InSb single crystal,[18] InSb made by melt spinning (MS) method,[19] $In_{0.9}Ga_{0.1}Sb$[20] compounds and InSb + 5 wt% CuCl.

The lattice thermal conductivity κ_L of the InSb + x wt% CuCl (x = 0, 3, 5, 8) samples, obtained by subtracting κ_e from the κ, are shown in Fig. 5(b). Similar to the thermal conductivity κ, the κ_L of all the samples decreases with increasing temperature. In the temperature range 313–650 K, the κ_L of all the samples follows well with the tendency of $\kappa_L \sim T^{-1}$, indicating that the phonon scattering is dominated by long acoustic phonons scattering.[23] However, In the temperature range of 313–650 K, the

κ_L of InSb + x wt% CuCl (x = 3, 5, 8) deviates from the T^{-1} tendency, indicating extra phonon scattering occurred. Combined with our XRD, EPMA and TEM results, we speculate it to the strengthened phonon scattering by hierarchical architectures at high temperature, including the atomic Cl_{Sb}^{2+} point defects, nanoscale Cu_9In_4 and Sb precipitates, as well as the mesoscale Cu_2Sb particles. In addition, it is noted that the InSb + x wt% CuCl (x = 0, 3, 5, 8) samples are stable at 600–733 K according to our C_p results, as shown in Fig. S4.

Figure 6(a) shows the ZT of InSb + x wt% CuCl samples. Due to the simultaneous optimization in PF and κ at 733 K, the ZT value of InSb was greatly improved, which increases from 0.22 for InSb to 0.77 for the $x = 5$ sample. Such an enhanced ZT is also much higher than other InSb based compounds reported in Refs. [18–20], as shown in Fig. 6(b).

In summary, we have demonstrated a simultaneous optimization in electrical and thermal properties of InSb by CuCl doping. It is found that CuCl can react with InSb during the SPS process, resulting in Cl to substitute Sb sites, and the formation of mesoscale Cu_2Sb, nanoscale Sb (∼50 nm) and Cu_9In_4 (10–20 nm). Consequently, CuCl doping enables us to achieve a high power factor of 31.5 μW·cm^{-1}·K^{-2} at 733 K and a low thermal conductivity of 2.99 W·m^{-1}·K^{-1} at 733 K for the InSb + 5 wt% CuCl sample. Eventually, due to simultaneous optimization in electrical and thermal properties, the peak ZT reaches a high value of 0.77 at 733 K for the InSb + 5 wt% CuCl sample, which is 250% higher than that of pristine InSb.

References

[1] Snyder G J and Toberer E S 2008 *Nat. Mater.* **7** 105
[2] Biswas K, He J, Blum I D, Wu C I, Hogan T P, Seidman D N, Dravid V P and Kanatzidis M G 2012 *Nature* **489** 414
[3] Zhao L D, Lo S H, Zhang Y, Sun H, Tan G, Uher C, Wolverton C, Dravid V P and Kanatzidis M G 2014 *Nature* **508** 373
[4] Zhou K, Zhang T, Liu B and Yao Y J 2020 *Chin. Phys. Lett.* **37** 017102
[5] Wang S F, Zhang Z G, Wang B T, Zhang J R and Wang F W 2021 *Chin. Phys. Lett.* **38** 046301
[6] Yan S, Wang Y, Gao Z, Long Y and Ren J 2021 *Chin. Phys. Lett.* **38** 027301
[7] Zhu G P, Zhao C W, Wang X W and Wang J 2021 *Chin. Phys. Lett.* **38** 024401
[8] Zhou L Y, Zheng Q, Bao L H and Liang W J 2020 *Chin. Phys. Lett.* **37** 017301
[9] Gao L, Liu Q, Yang J, Wu Y, Liu Z, Qin S, Ye X, Jin S, Li G, Zhao H, Long Y 2020 *Chin. Phys. Lett.* **37** 066202
[10] Qin B C, Wang D Y, Liu X X, Qin Y X, Dong J F, Luo J F, Li J W, Liu W, Tan G J, Tang X, Li J, He J and Zhao L 2021 *Science* **373** 556
[11] Feng B, Li G Q, Hu X M, Liu P H, Li R S, Zhang Y L, Li Y W, He Z and Fan X A 2020 *Chin. Phys. Lett.* **37** 037201
[12] He W, Qin B and Zhao L D 2020 *Chin. Phys. Lett.* **37** 087104
[13] Ma Z, Xu T, Li W, Cheng Y, Li J, Zhang D, Jiang Q, Luo Y and Yang J 2021 *Adv. Funct. Mater.* **31** 2103197
[14] Luo Y, Hao S, Cai S, Slade T J, Luo Z Z, Dravid V P, Wolverton C, Yan Q and Kanatzidis M G 2020 *J. Am. Chem. Soc.* **142** 15187
[15] Cai S, Hao S, Luo Y, Su X, Luo Z Z, Hu X, Wolverton C, Dravid V P and Kanatzidis M G 2020 *Chem. Mater.* **32** 3561
[16] Luo Y, Cai S, Hao S, Pielnhofer F, Hadar I, Luo Z Z, Xu J, Wolverton C, Dravid V P, Pfitzner A, Yan Q and Kanatzidis M G 2020 *Joule* **4** 159
[17] Bowers R, Ure R W, Bauerle J E and Cornish A J 1959 *J. Appl. Phys.* **30** 930
[18] Yamaguchi S, Matsumoto T, Yamazaki J, Kaiwa N and Yamamoto A 2005 *Appl. Phys. Lett.* **87** 201902
[19] Su X L, Tang X F and Han L 2010 *Acta Phys. Sin.* **59** 2860 (in Chinese)
[20] Zhang Q, Xiong Z, Jiang J, Li W, Xu G, Bai S, Cui P and Chen L 2011 *J. Mater. Chem.* **21** 12398
[21] Mao J, Niedziela J L, Wang Y, Xia Y, Ge B, Liu Z, Zhou J, Ren Z, Liu W, Chan M K Y, Chen G, Delaire O, Zhang Q and Ren Z 2018 *Nano Energy* **48** 189
[22] Cheng Y, Yang J, Jiang Q, He D, He J, Luo Y, Zhang D, Zhou Z, Ren Y and Xin J 2017 *J. Mater. Chem. A* **5** 5163
[23] Xin J, Jiang Q, Wen Y, Li S, Zhang J, Basit A, Shu L, Li X and Yang J 2018 *J. Mater. Chem. A* **6** 17049
[24] Luo Y, Yang J, Jiang Q, Li W, Zhang D, Zhou Z, Cheng Y, Ren Y and He X 2016 *Adv. Energy Mater.* **6** 1600007
[25] Zhao L D, Lo S H, He J, Li H, Biswas K, Androulakis J, Wu C I, Hogan T P, Chung D Y, Dravid V P and Kanatzidis M G 2011 *J. Am. Chem. Soc.* **133** 20476
[26] Tan G, Stoumpos C C, Wang S, Bailey T P, Zhao L D, Uher C and Kanatzidis M G 2017 *Adv. Energy Mater.* **7** 1700099
[27] Suwardi A, Bash D, Ng H K, Gomez J R, Repaka D V M, Kumar P and Hippalgaonkar K 2019 *J. Mater. Chem. A* **7** 23762
[28] Bouarissa N and Aourag H 1999 *Infrared Phys. Technol.* **40** 343
[29] Hee K J, Jae K M, Oh S, Rhyee J S, Park S D and Ahn D 2015 *Dalton Trans.* **44** 3185

Supplementary Material for "Simultaneous optimization of power factor and thermal conductivity towards high-performance InSb-based thermoelectric materials"

Wang Li(李旺) Tian Xu (许天) Zheng Ma (马征), Qing-Hui Jiang (姜庆辉) Yu-Bo Luo (罗裕波), Jun-You Yang (杨君友)**

State Key Laboratory of Materials Processing and Die & Mould Technology
Huazhong University of Science and Technology, Wuhan 430074, P. R. China

1. The synthesis, characterization and measurement methods of the InSb + *x* wt.% CuCl (*x* = 0, 3, 5, 8) samples.

The InSb samples were prepared with nominal stoichiometric ratio, followed by high temperature (923K) melting in the evacuated quartz tubes. The obtained ingots were crushed into fine powder and passed through 200-mesh sieve to ensure the initial powder at the same size. Later, CuCl powder was added into InSb substrate with different weight ratio *x*% (*x* = 0, 3, 5, 8). Subsequently, the mixture was loaded into graphite mold and densified by Spark Plasma Sintering (SPS) under a pressure of 60 MPa in vacuum atmosphere to get compact wafers. Electrical resistivity and Seebeck coefficient were acquired simultaneously in high vacuum using a Namicro-III thermoelectric measurement system. Hall carrier concentration and mobility measurement were performed on Hall Effect Measurement System (ECOPIA HMS-5500) with Van der Pauw method. The thermal conductivity was calculated by $\kappa = C_p D \rho$, where heat capacity (C_p) was obtained by differential scanning calorimetry (DSC25, TA Inc.) thermal diffusion coefficient (D) was determined by the laser flash methods in the flowing N_2 atmosphere with a LFA-427(NETZSCH) equipment, density (ρ) was obtained by the Archimedes' method.

Phase and compositions were characterized by PANalytical X'pert PRO diffractometer, followed by Rietveld refinement using the GSAS+EXGUI software. electron probe microanalyzer (EPMA) (EPMA-8050G, Shimadzu) equipped with energy-dispersive X-ray spectroscopy (EDS) was applied to analyze the microstructure and elements distribution of the polished surfaces of InSb + 8 wt.% CuCl sample. High resolution transmission electron microscopy (HRTEM) observation was carried out on a Talos F200X microscope at an accelerating voltage of 200kV.

2. The calculation details of estimating Lorenz number and electron effective mass

$$L = (\frac{k_B}{e})^2 \{\frac{(r+7/2)F_{r+5/2}(\eta)}{(r+3/2)F_{r+1/2}(\eta)} - [\frac{(r+5/2)F_{r+3/2}(\eta)}{(r+3/2)F_{r+1/2}(\eta)}]^2\} \quad \textbf{(S1)}$$

$$F_n(\eta) = \int_0^\infty \frac{\chi^n}{1+e^{\chi-\eta}} d\chi \quad \textbf{(S2)}$$

$$\eta = \frac{F_f}{k_B T} \quad \textbf{(S3)}$$

$$S = \pm \frac{k_B}{e} (\frac{(r+5/2)F_{r+3/2}(\eta)}{(r+3/2)F_{r+1/2}(\eta)} - \eta) \quad \textbf{(S4)}$$

$$m^* = \frac{h^2}{2k_B T} (\frac{n}{4\pi F_{1/2}(\eta)})^{2/3} \quad \textbf{(S5)}$$

Where the integral $F_n(\eta)$ is Fermi integral function with order n, and the η is reduced Fermi level, defined as **Eq S3** and can be obtained with the measured Seebeck coefficient by **Eq. S4.** The scattering factor can be considered as -1/2 when regarding to acoustic phonons scattering. Therefore, the electron effective mass can be estimated with the measured carrier concentration according to the **Eq. S5**. Where T, k_B and h are temperature (300K), Boltzmann' constant and Planck' constant.

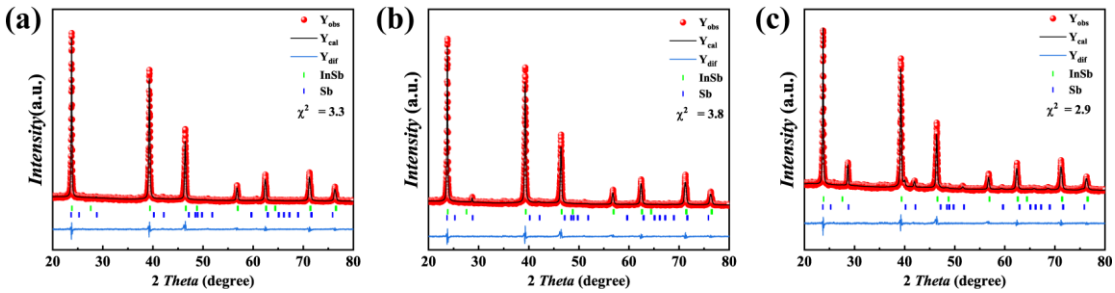

Fig.S1 Rietveld refinement results for *x* = 3, 5, 8 samples.

Table.S1 Results of Rietveld refinements of PXRD patterns for InSb + 5 wt.% CuCl at room temperature

Samples			***x* = 3**	***x* = 5**	***x* = 8**
Chi^2			3.3	3.8	2.9
a(A)			6.4704	6.4720	6.4701
Cycles			771	744	862
Frac(%)		**InSb**	99.69±0.12	96.88±0.13	93.89±0.45
		Sb	0.3±0.08	3.1±0.15	6.0±0.15
GW		**InSb**	-2.0e1	-9.1e0	2.47e1
		Sb	1.1e1	-1.01e2	-8.0e2
Shft		**InSb**	-1.1e0	1.29e0	2.46e0
		Sb	1.4e0	-1.25e0	-5.83e0
Uiso	**InSb**	**In**	6.66e-3	9.43e-3	-6.4e-3
		Sb	4.1e-3	8.01e-3	6.39e-3
	Sb		0.01	0.01	0.01

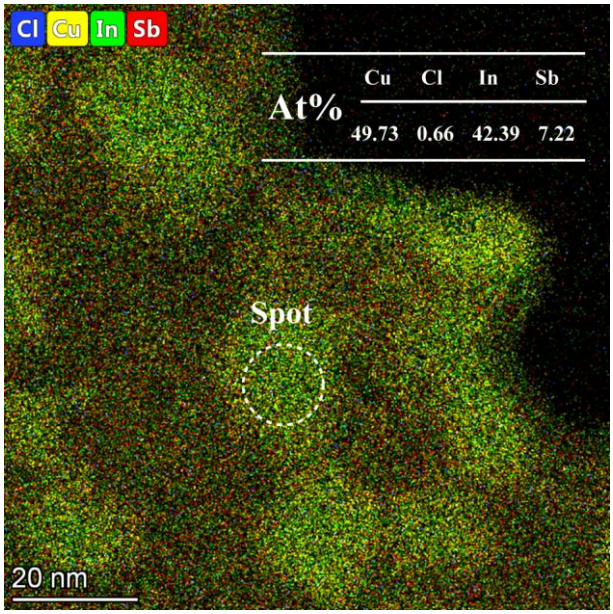

Fig. S2 Elements distribution in of panel **Fig 3d**

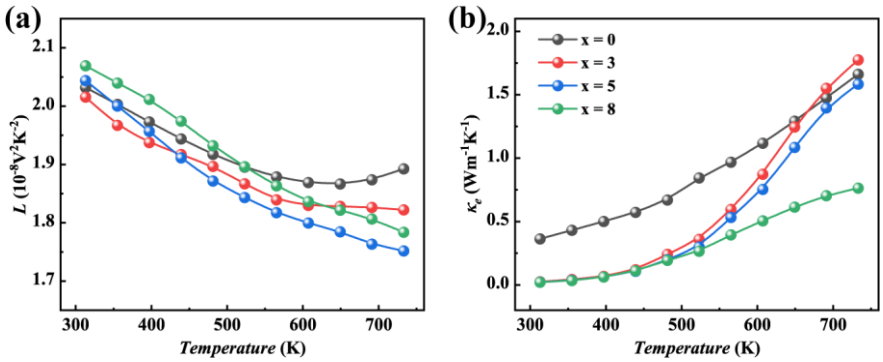

Fig.S3. (a) Lorenz number estimation with **Eq.S1**; (b) temperature dependent κ_e of InSb + *x* wt.% CuCl (*x* = 0, 3, 5, 8).

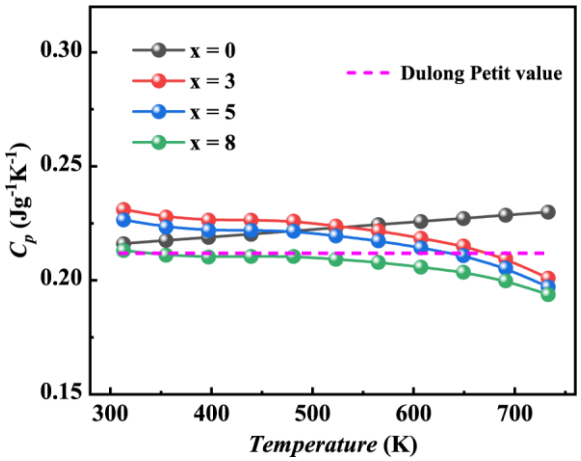

Fig.S4 The heat capacity of InSb + *x* wt.%CuCl (*x* = 0, 3, 5, 8) samples.